

The asymmetric structure of the Galactic halo

Y. Xu^{1,2*}, L. C. Deng^{1*} and J. Y. Hu^{1*}

¹*National Astronomical Observatories, Chinese Academy of Sciences, Beijing 100012, P. R. China*

²*Graduate University of Chinese Academy of Sciences, Beijing, 100049, P. R. China*

15 August 2018

ABSTRACT

Using the stellar photometry catalogue based on the latest data release (DR4) of the Sloan Digital Sky Survey (SDSS), a study of the Galactic structure using star counts is carried out for selected areas of the sky. The sample areas are selected along a circle at a Galactic latitude of $+60^\circ$, and 10 strips of high Galactic latitude along different longitudes. Direct statistics of the data show that the surface densities of ℓ from 180° to 360° are systematically higher than those of ℓ from 0° to 180° , defining a region of overdensity (in the direction of Virgo) and another one of underdensity (in the direction of Ursa Major) with respect to an axisymmetric model. It is shown by comparing the results from star counts in the $(g-r)$ colour that the density deviations are due to an asymmetry of the stellar density in the halo. Theoretical models for the surface density profile are built and star counts are performed using a triaxial halo of which the parameters are constrained by observational data. Two possible reasons for the asymmetric structure are discussed.

Key words: Stars: statistics – the Galaxy: structure, fundamental parameters, halo

1 INTRODUCTION

It has been one of the central goals of human knowledge to understand the position of the Earth in the universe. A lot of effort has been spent to derive the structure and the history of formation and evolution of our Galaxy. Doing this is a particularly difficult task, simply because there is no good viewpoint, as opposed to the case for external galaxies whose structures can be observed directly. The structure, formation and evolution of the Galaxy are very important issues in contemporary astrophysics; they are closely related to stellar quantities such as distance, age, metallicity, and kinematics of the individual stars, among others. These properties can be obtained for large stellar samples using straightforward photometric and spectroscopic observations. In the present era, before the full exploitation of the planned huge spectral surveys of Galactic stellar objects (e.g. GAIA, SEGUE, 6dF, LAMOST) is possible, using star counts based on all-sky photometric surveys is a direct and one of the few accessible methods for the study of the structure of the Galaxy.

Probing the Galaxy using star counts has a history of about 200 years (Reid 1993), with the modern epoch marked by the classic work of Bahcall & Soneira (1980), based on several observations (Seares et al. 1925, Kron 1978, Tyson & Jarvis 1979, Peterson, Ellis & Kibblewhite 1979). Bahcall & Soneira built a standard model, in which the Galaxy was

simplified and parameterized by an exponential disk and a spheroid characterized by a de Vaucouleurs profile. Assuming a density profile for each population, based on detailed studies of nearby spiral galaxies, and assuming a luminosity function as observed for stars in the local volume, their model predicts number density – magnitude – colour distributions.

Further studies on this subject provided certain modifications to the Bahcall & Soneira model. Theoretical models were further constrained using new observations were subsequently obtained. In 1984, Gilmore claimed for the first time that there is a thick disk in our Galaxy. The star counts approach to the study of the structure of the Galaxy was extensively reviewed by Reid (1993); he, and his colleagues, (Reid 1993, Reid, Yan & Majewski 1996, Majewski, Siegel & Kunkel et al. 1999, Siegel, Majewski & Reid 2002) carried out a series of studies appropriately termed “star counts redivivus”, dedicated respectively to: faint magnitude star counts, the halo luminosity function, and an exploration of the contamination of star counts by star streams. When the Sloan Digital Sky Survey (SDSS) made its first data release publicly available, it raised very promising prospects for the study of Galactic structure thanks to the large sky coverage and the deep stellar photometry. Chen et al. (2001) analysed the SDSS early data release (EDR); they confirmed the existence of a Galactic thick disk and obtained a set of structural parameters for the Galaxy. With the increasing sky coverage in subsequent SDSS data releases, it is expected that one will be able to determine the Galactic structure parameters

* E-mail: xuyan@bao.ac.cn(YX); licai@bao.ac.cn(LCD); hjy@bao.ac.cn(JYH)

ever more precisely. Except for constraining the density profile, the stellar luminosity function can also be determined with a higher accuracy. In Gould, Bahcall & Flynn (1996), and Zheng, Flynn & Gould (2001, 2004) the disk M-dwarf and *I*-band luminosity functions are obtained using *Hubble Space Telescope* star counts. In Reid (2002), the luminosity function in the solar neighborhood was studied based on the Palomar/MSU nearby star spectroscopic survey.

The Galactic structural parameters derived from various studies show large divergence, which cannot simply be attributed to statistical errors, although these are generally significant. In star counts from fields selected following a certain symmetry approach, there are deviations from the axisymmetric standard model which are obvious and cannot be neglected. Spergel & Blitz (1988) pointed out that this might be an indication of a triaxial structure of the Galaxy, and they used a triaxial halo to explain the asymmetries detected from gas motions around $\ell=180^\circ$. Later, Blitz & Spergel (1991) showed that the observed HI gas is moving in an asymmetric gravitational potential. Using areas selected from the ASP catalogue, Larsen & Humphreys (1996) found deviations of star counts from the axisymmetric model; they found that there are significant excesses of stars in quadrant I, at $l = 20^\circ - 50^\circ$, compared to quadrant IV, around $b = 30^\circ$. Further work was published by Parker, Humphreys & Larsen (2003), who compare star counts in 120 POSS I fields. They claimed that the excess is not associated with any known stream such as those linked to the Sagittarius dwarf, Magellanic stream or Fornax-Leo-Sculptor stream. Parker, Humphreys & Beers (2004), however, concluded that the excess is due to thick disk stars and may be associated with the recently discovered Canis Major debris stream. In Hartwick (2000), possible reasons for causing triaxiality due to nearby spiral and dwarf galaxies are considered. Newberg & Yanny (2005b) built triaxial ellipsoidal stellar halo models and analysed F turn-off star samples from SDSS DR3.

To explain the observed excess of the stellar number density with respect to an axisymmetric halo, two competing scenarios have been proposed: the triaxiality could be an inherent property related to the smooth structure of the Galaxy, or it could be related to the remnants of some historical merger events. Recently, this debate has intensified with the reported “Virgo overdensity” by Jurić et al. (2005), which may be the cause of the large-scale asymmetry in the structure of the Galaxy. By using the photometric parallax method, they measured stellar distances which allowed them to construct a map of the 3D structure of the sky area covered by current SDSS survey. Their study has, for the first time, revealed large-scale patterns in the Galaxy. In the same data that showed the Virgo overdensity, an underdense area with respect to an axisymmetric halo model is also obvious in the direction of UMa. Whereas the overdensity can be naturally interpreted as a large-scale star stream in the halo model, the UMa underdensity cannot be accounted for in the same way. We believe that this observational fact is linked to the smooth structure of the halo in which the star streams (including the Virgo overdensity) are embedded. To tackle this problem, a similar star count analysis of Galactic structure will be followed in this paper.

The Sloan Digital Sky Survey is a five-colour (u, g, r, i, z) broad-band photometric survey with a wavelength coverage from 3000 to 11,000Å (Fukugita, Ichikawa

& Gunn 1996). The DR4 imaging catalogue covers 6670 square degrees. Its detection repeatability is complete at a 95% level for point sources brighter than the limiting apparent magnitudes of 22.0, 22.2, 22.2, 21.3 and 20.5 for u, g, r, i and z , respectively (<http://www.sdss.org>). It has facilitated great progress in the study of the structure of the Galaxy, which was reviewed in the SDSS-II SEGUE Project. For the study of Galactic structure using star counts, SDSS provides the most up-to-date and complete stellar sample in terms of both sky coverage and magnitude limit. Thus, the SDSS is suitable to study the large-scale asymmetry of the Galaxy. In this paper, we build a model of the Galaxy with a non-axisymmetric geometry, and constrain the parameters of the model using observations in a set of characteristic directions taken from SDSS DR4. In Section 2, the selected observational data are described. In Section 3, the model used to fit the observational data is introduced. The results of triaxial halo model and the asymmetric structure of the Galaxy are described and analysed in Section 4. A discussion of the present results and our conclusions are given in the final section.

2 OBSERVATIONAL DATA

The SDSS is based on observations obtained with a 2.5m telescope with a 3° field of view at the Apache Point Observatory in New Mexico, USA. Standard operations of the SDSS were performed from 2000 to 2005. Eventually, it will cover π steradians centred on the northern Galactic cap and three stripes near the southern Galactic cap (Stoughton, Lupton & Bernardi 2002). The operating mode of observations is by means of drift scanning. One continuous scan is designated by a “run”, and two such runs generate a “stripe”; they have an overlap region of 1 arcmin on the edges of the two scans (Chen et al. 2001). Catalogues of objects classified as “stars” from DR4 were downloaded from the sky server for sky areas selected to meet our aims. The retrieved data is free of overlap and has been deblended; saturated stars and poor-quality objects near bright stars and the edges of the frames were all filtered out (Newberg & Yanny 2005b).

If the Galaxy is axisymmetric, as usually assumed in previous studies, the projected stellar number density at the same Galactic latitude will increase towards the direction of $\ell = 0^\circ$, and decrease when approaching $\ell = 180^\circ$, and any sky area pair mirror-symmetrically selected on either side of the $\ell = 0^\circ$ meridian plane should retrieve the same star number counts, within the uncertainties. If the axisymmetric model is correct, such a picture should be reproduced by star counts across the whole sky area, and can in principle also be detected in symmetrically selected subsets of sky areas. Limited by the current SDSS sky coverage, whole-sky star counts are not possible, but a uniform data set covering all longitudes at a given latitude should suffice, as this would be a perfect probe to check the axisymmetric assumption. Such a data set is now available from SDSS DR4, which will be addressed in the following. Fig. 1 is a Lambert projection of the northern Galactic hemisphere, showing the selected sky areas used in this work (marked by diamonds). Each of the selected sky areas has a size of about $2^\circ \times 2^\circ$; the Galactic coordinates of the centres of the selected fields are given

in Table 1. The sky areas selected along the circle at $b = 60^\circ$ form the first group of our working data set. To check the structure at latitudes different from $b = 60^\circ$, sky area pairs at different latitudes (from $b = 55^\circ - 85^\circ$, equally spaced by 5°) along our longitudinal grid (in steps of 30° from 0 to $\sim 360^\circ$) are also selected. In order to minimise the effects of extinction, sky areas below $b = 55^\circ$ were excluded. From the present SDSS public data release, sky areas of 11 longitudinal strips are available, and selected field from these form the remaining 11 data groups in our sample. From the second to the twelfth group, the sky areas within each group have the same longitude, so that the structural properties reflected by the stellar number densities along a given longitude can be derived. In addition, through comparison between sky areas having mirror symmetry with respect to the $\ell = 0^\circ$ meridian deviations from the axisymmetric Galaxy model can also be checked. Owing to the SDSS observing strategy, stars brighter than 15^m will be saturated, and star counts will be not complete for magnitudes fainter than $22^m.2$ in the g and r bands, so that our work will be limited in the range of magnitudes from 15^m to 22^m in both the g and r bands.

3 THE THEORETICAL MODEL

To fully reveal the structure of the Milky Way, accurate measurements of the distances to individual objects are key ingredients. Such information is still lacking at the present time, however. As a consequence, the structure of the Galaxy cannot be resolved satisfactorily. Very large-scale photometric surveys greatly improve our knowledge of Galactic structure. However, the problem remains even if we use the data generated by the SDSS project, because of our inability to determine stellar distances accurately. The major science drivers of the SDSS are focused on extragalactic objects. Therefore, a wide-filter photometric system was designed to detect the faintest possible extragalactic objects. The narrowest filter, u , is 600\AA . Such a photometric system has an obvious disadvantage when one wants to measure absolute stellar magnitudes, compared with the classical $ubv\gamma\beta$ system. The latter system by itself is already characterised by a scatter of 0.3 mag for A and F-type stars (Crawford 1975, 1979). The difficulty to distinguish between giant and main-sequence stars will affect counts of G and K-type stars even more seriously in the SDSS system if one applies the colour-magnitude relation for main-sequence star to all stars. Furthermore, the large range of metallicity that is intrinsically present in the sample will inherently lead to large scatter in the colour-magnitude relation. To obtain distances to stars and to determine the structure of the Galaxy directly from SDSS data is thus somewhat difficult. A preliminary approach to this problem using the photometric parallax method and its pitfalls are carefully analysed by Jurić et al. (2005).

To derive the structure of the Galaxy from the integrated stellar light distribution along the line of sight, a theoretical model is needed. Our Galactic disk models follows is based on that of Bahcall & Soneira (1980), while we have also included a thick-disk component. Because of large deviations from an axisymmetric structure (described in Section 4), we have modified the standard axisymmetric

halo; these deviations will be accounted for by a triaxial halo instead.

The basic star count equation we use is:

$$A(M_1, M_2, \ell, b) = \int_{M_1}^{M_2} dM' \int_0^\infty R^2 dR \rho(\mathbf{r}) \phi(M) d\Omega, \quad (1)$$

where $A(M_1, M_2, \ell, b)$ is the projected surface density in the absolute magnitude bin from M_1 to M_2 in the direction of Galactic longitude ℓ and Galactic latitude b ; R is the heliocentric distance of a given star; $\rho(\mathbf{r})$ is the density profile of each stellar population as a function of \mathbf{r} , the distance to the Galactic Centre; $\phi(M)$ is the luminosity function of each contributing stellar population, which is a function of absolute magnitude and $d\Omega$ is the solid angle element covered by the observations.

For the thin and thick disk components, the density profile is assumed to be of the following exponential form,

$$\rho(\mathbf{r}) = \exp[-|z|/H - x/h], \quad (2)$$

where z is the height above the Galactic plane, x the projected distance to the Galactic Centre in the Galactic plane, and H and h are the scale height and scale length in z and x , respectively. As this study focuses on the structure of the halo, we used fixed models for both the thin and the thick disks, so that complications due to extra free parameters for these disks can be excluded. The parameters of the disks are taken from Chen et al. (2001). For the thin disk, $H = 330$ pc and $h = 2.25$ kpc; for the thick disk, $H = 650$ pc and $h = 3.5$ kpc. The galactocentric distance of the Sun is $r_0 = 8.5$ kpc, and the vertical distance of the Sun from the Galactic disk plane is $z_0 = 27$ pc.

For the halo, a triaxial model is adopted to fit the observational data. A set of suitable coordinate frames is built following Newberg & Yanny (2005b), of which the schematic diagram is shown in Fig. 2. Adopting the position of the Sun as the origin of the coordinate frame, the direction from the Sun to the Galactic Centre is taken as the x -axis. The y -axis is the direction perpendicular to the x -axis in an anticlockwise sense within the Galactic plane, while the z -axis coincides with the direction towards the northern Galactic pole. The x' and y' directions are parallel to x and y , but their origin is at the Galactic Centre instead; these axes also define a right-handed coordinate system. Furthermore, R is the distance from a star to the Sun, r the distance from the star to the Galactic Centre and t is the projection of r on the Galactic plane. Therefore, $z = R \times \sin(b) + z_0$, $z_0 = 27$ pc, $t = \sqrt{r_0^2 + R^2 - 2 \times R \times r_0 \times \cos(b) \times \cos(l)}$. The Galactic Centre coordinate frame is rotated in such a way that its axes are settled right on the three axes of the triaxial ellipsoid. The transformation between the coordinate frames can be separated into three rotational steps: first, fix arbitrarily one of the three axes and rotate the other two. The rotation angles of the three steps, denoted by θ , ξ and ϕ , are defined when fixing the z , x and y axes, respectively. In Fig. 2, for example, where we rotate x' and y' around the z' axis, the relevant transformations are, $x_1 = x' \times \cos(\theta) + y' \times \sin(\theta)$, $y_1 = -x' \times \sin(\theta) + y' \times \cos(\theta)$, and $z_1 = z'$. The remaining two steps involve doing the same for the other two axes. The new axes obtained after the third rotation are (x_3, y_3, z_3) , and the three axes of the triaxial ellipsoid are a, b and c , where a is the longest and c the shortest axis. The axis ratios of the triaxial ellipsoid are

$p = b/a$, and $q = c/a$, while $r = \sqrt{x_3^2 + (y_3/p)^2 + (z_3/q)^2}$. The axisymmetric halo is described by $p = 1$.

A power-law (Reid 1993) is adopted for the halo density distribution,

$$\rho(\mathbf{r}) = \frac{a_0^n + r_0^n}{a_0^n + r^n}, \quad (3)$$

where $a_0 = 1000$ is a normalisation constant. We adopt the V -band luminosity function of Robin & Créé (1986) in our model, which provides sufficiently accurate two-dimensional distributions in both luminosity and spectral type down to $V = 12$ mag. A two-dimensional V -band luminosity function can easily be transformed to that in the g band. Robin & Créé (1986) compiled a number of luminosity functions available at the time, including those of Wielen (1974, 1983) and Houk & Cowley (1975, 1978, 1982). The work of Wielen is widely used in star count studies to obtain number density-magnitude relations for $2 \leq M_V \leq 12$ mag, while Houk & Cowley's luminosity function is often used for the bright stars ($-2 \leq M_V \leq 2$ mag). Deutschman, Davis & Schild (1976) and Hayes (1978) provided calibrations of stellar luminosity and spectral type. To deal with the data used for the present study, a further transformation relation (Chen et al. 2001) from V to g , $g = V + 0.53(B - V) - 0.075$, was also adopted.

By using the density profile and the luminosity function discussed and presented above, the distribution in absolute g magnitude of the stellar projected surface number density can be obtained from Eq. (1).

A colour-magnitude relation (CMR) is needed to obtain the number density distribution in the $(g - r)$ colour. It is usual practice to use the CMR defined by colour-magnitude diagrams (CMDs) of star clusters. However, there are usually too few stars in cluster CMDs with absolute magnitudes fainter than 10^m . Therefore, at fainter magnitudes we do not have a precise CMR. As an alternative approach, we adopt the theoretical isochrones of Girardi, Grebel & Odenkirchen (2004) to derive the CMR required here. The mean ages of thin disk, thick disk and halo are assumed to be 4.5, 11 and 13 Gyr, and their metallicities are assumed to be, respectively, 0.019, 0.004 and 0.0012. The theoretical CMR is preferred because it includes faint stars that are otherwise not available from observations. However, we have to bear in mind that it cannot mimic the scatter on the relation in real situations.

Given a theoretical model for stellar distributions of different Galactic components as described above, it is straightforward to calculate the projected surface number density in absolute magnitude bins in any given direction. From observations, the information that can be directly extracted is the projected surface number density in apparent magnitude bins. The goal of the present study is to use this information to constrain the structure of the Galaxy parameterised in the manner explained above.

A Monte Carlo method was adopted to simulate the observational statistics. Random points were generated based on several quantities, including the luminosity function, distances weighted by the input density profile, and a Gaussian-type observational error, so that the observed star counts can be reproduced. For these simulations, we adopted the three-dimensional extinction model of the Milky Way derived from COBE observations (Drimmel, Cabrera-Lavers &

López-Corredoira 2003). Instead of correcting the observational data for the very complicated interstellar reddening, we applied reddening corrections to the stellar distributions predicted by the model. The extinction, A_V , is in general small throughout the areas selected in this study, with a maximum of about 0.104 mag in the direction (0° , 55°) and a minimum of 0.0385 mag in the anti-Galactic Centre direction ($b = 80^\circ$), at a distance of about 600 pc along the line of sight. A_V is obtained through linear interpolation for distances less than 600 pc. For greater distances, A_V is taken to be constant. The g -to- V -band extinction ratios were taken from Girardi et al. (2004), and thus we can also obtain the apparent g and r -band magnitudes at each theoretical point.

We can now calculate the theoretical projected surface number density, theoretical star counts as a function of apparent g and r magnitude, and theoretical star counts as a function of $(g - r)$ colour down to the SDSS limiting magnitudes, and hence we are now ready to compare these with the observational data.

4 RESULTS AND ANALYSIS

4.1 Analysis of the first group of observational data at $b=60^\circ$

The discrete small sky areas of group 1, covering a complete circle at the Galactic latitude of $b=60^\circ$, form a unique probe of the structure of the Galaxy in the current SDSS data release. Direct measurements of the stellar number density distribution within this data set can tell us whether or not it is axisymmetrical.

We tested this idea by fitting the surface density distribution along the circle with an axisymmetric halo. Fig. 4 shows the projected surface number density distributions of the theoretical model and the observational distribution for stars of $g, r \in [15, 22]$ mag, where the diamonds represent the observational projected stellar surface number density. To account for observational fluctuations, each sky field was divided into four subfields of $1^\circ \times 1^\circ$ (except for the area $[200^\circ, 60^\circ]$, which is too small for this procedure), so that the statistical fluctuations can be measured. The resulting fluctuations over the average of the four subfields are shown in the figure as error bars on the data points. The dashed line is the theoretical prediction for an axisymmetric model. The dashed theoretical line was normalised by taking the average values of the surface density at $(0^\circ, 60^\circ)$ and $(180^\circ, 60^\circ)$ from the observational data. It is worthwhile to point out that the two parts of the dashed theoretical line, i.e., that between $\ell = 0^\circ$ and 180° , and that between 180° and 360° , are not perfectly symmetrical because of extinction. In addition, due to the non-uniform extinction, the surface number density curves shown in Fig. 4 are not smooth. It is evident that the axisymmetric model does not fit the observations very well. Comparing the observational data with the axisymmetric model prediction, it is obvious that the observational data between $\ell = 0^\circ$ and 180° on the one hand, and between $\ell = 180^\circ$ and 360° on the other are highly asymmetrical; the projected surface density in the fields at $\ell > 180^\circ$ is systematically higher than that in the fields mirror-symmetrically located on the other side of the meridian. The axisymmetric theoretical value is a little higher

than derived from the observations for longitudes from 0° to 180° , and much lower than implied by the observational data for $\ell = 180^\circ$ to 360° . The deviations from the axisymmetric model are rather smooth; they seem to represent a systematic shift from the theoretical model.

To find out what kind of stars are responsible for these asymmetric statistics, we performed a number of tests. In Table 2 we list the star counts of stars with $g, r \in [15, 22]$ mag in the paired sky fields selected symmetrically with respect to the 0° meridian plane, as well as the relative fluctuations (defined as [surface density of ℓ_2 - surface density of ℓ_1]/[surface density of ℓ_1], where ℓ_1 and ℓ_2 are the Galactic longitudes of the paired fields). In Table 3, faint stars with $g, r \in [19, 21]$ mag are considered in the same way. They show the same trend as the previous data set, resulting in an uneven distribution with an even higher asymmetric ratio.

In Fig. 3, star counts in four colours, $(u - g)$, $(g - r)$, $(r - i)$ and $(i - z)$, in the fields towards the directions of $(90^\circ, 60^\circ)$ and $(270^\circ, 60^\circ)$ are compared. The magnitude ranges are, respectively, $15 \leq u \leq 22$, $15 \leq g \leq 22$, $15 \leq r \leq 22$, $15 \leq i \leq 21$, and $15 \leq z \leq 20$. In each of the colour distribution profiles there are two peaks, as shown in Fig. 3 (the blue tail at $(u - g) \sim 0.1$ is mostly due to white dwarf stars). The left-hand peak is dominated by halo stars, while the one on the right is dominated by thin disk stars, as inferred from the colours. This is because most of halo stars are far more distant than the bulk of the disk stars, and therefore only the luminous stars in the halo (predominantly main-sequence stars) can be detected. For stars on the main sequence, the intrinsically brighter ones have bluer colors. In addition, the halo stars are generally more metal poor, and hence tend to populate the blue peak. Based on a similar argument related to the stellar metallicity, thin disk stars would form the red peak. Therefore, it is clear that the excess of the stellar number density in the field at $(270^\circ, 60^\circ)$ with respect to that at $(90^\circ, 60^\circ)$ is due to the halo component. The amplitude of the excess depends on colour, as shown in Fig. 3; it is larger in $(u - g)$, $(g - r)$ and $(r - i)$ than in $(i - z)$. It may be caused by the different limiting magnitudes, or it might be an indication of the specific properties of the stars that causes the excess.

4.2 Fitting the projected surface number densities with a triaxial halo model

A triaxial halo model, as described in Section 3, is adopted to describe the asymmetry found in our data set. Given the same limiting magnitudes as those of the observations, the theoretical surface densities are calculated using a model of which the structural parameters are constrained by a comparison with the observations.

The three-component model (including the thin and thick disks, and the halo) is used to calculate projected surface number densities in the sky areas corresponding to those of the observations. As the main objective of the current work is to derive the structure of the halo, for the parameters of the thin and thick disk we adopt the results of Chen et al. (2001). The parameters of the halo are adjusted in such a way that the observational data are best fitted. The integration of the observational surface density over all of

the selected fields is used to constrain the surface density of the model.

There are a total of six parameters in our halo model, namely the power-law index n , the two axis ratios p and q , and the three coordinate rotation angles ξ , ϕ , θ (based on which the x, y, z axes of the triaxial ellipsoidal model can be translated to that of the Galaxy). The possible ranges of the parameters are estimated using initial tests over a preliminary grid, which is given in Table 4.

Chi-squared minimisation tests comparing the theoretical and observational data sets were carried out using the algorithm of Press et al. (1992). For a non-Gaussian distribution of discrete data points, Pearson's χ^2 can be expressed as,

$$\chi^2 = \sum_{i=1}^N \frac{(R_i - S_i)^2}{(R_i + S_i)(N - m)}, \quad (4)$$

where R_i is the theoretical frequency of data points in the i^{th} bin, and S_i is the equivalent frequency of the observations. N is the number of bins, m the number of model parameters, and therefore $(N - m)$ is the number of degrees of freedom. Assuming that the errors in the theoretical and observational frequencies are distributed in a Poissonian fashion, we obtain $\sigma^2 = (\sqrt{R_i^2} + \sqrt{S_i^2})^2$. By changing the model parameters, the parameter combination that generates the minimum averaged χ^2 of the 12 groups can be obtained.

Models for all possible combinations of the six parameters were calculated, and the corresponding χ^2 s were evaluated to find the parameter combination resulting in the minimum χ^2 value. It is obvious that the models with (p, q) in the range of $(0.5, 0.5)$, $(0.6, 0.5)$, $(0.7, 0.6)$, and $(0.8, 0.6)$ lead to better values for χ^2 , regardless of any fine-tuning of the other four parameters. The models provide only weak constraints for the power-law index n . When n is fine-tuned, the axial ratio should be adjusted accordingly, in order to obtain the optimum χ^2 . The overall trend is that for larger n , larger p or q ratios are needed.

Figs 4 and 5 show the observational surface densities in the selected regions and those of our theoretical models calculated by using a triaxial halo with the following parameter combination, $n = 2.2, p = 0.5, q = 0.5, \theta = 60^\circ, \xi = -10^\circ$, and $\phi = -10^\circ$, and the corresponding χ^2 is 2.02. (This is the parameter set that leads to the minimum $\overline{\chi}_{g-r}^2$, see Section 4.3 for more details). Fig. 4 shows the results for the group-1 fields, spanning a circle at $b = 60^\circ$. A comparison between the solid and dashed lines in Fig. 4 shows that the triaxial halo model (the solid line) fits the observations much better than an axisymmetric halo (the dashed line), with the triaxial halo clearly showing the degree of asymmetry as revealed by the observations. The only sizable deviations of the triaxial model from the observations are found near $\ell = 260^\circ$ (where the theoretical prediction for the surface density is slightly higher), and near $\ell = 330^\circ$ (where the theoretical value is somewhat lower). The six panels in Fig. 5, labelled A-F, show the surface densities of both the observations (diamonds and triangles) and the models (dotted and dashed lines) for groups 2 to 12. Panel A shows the surface densities in the fields at $\ell=0^\circ$ and $\ell=180^\circ$ as a function of Galactic latitude. Panels B through E show the surface densities in the sky-field pairs mirror-symmetrically selected on either side of the 0 degree Galactic meridian plane. Panel F de-

picts that in the $\ell=150^\circ$ field, the companion field of which is not shown because the data has not yet been released. From these figures, it is clear that there are larger surface densities in the sky areas between $\ell = 180^\circ$ and 360° than in their corresponding mirror-symmetric fields. These fields thus show the same trend as the sky areas in the first group, at $b = 60^\circ$. The theoretical model fits the observations quite well in general, with several exceptions. For the three groups at $\ell=0^\circ, 240^\circ$, and 270° , the values are higher than those of the observations around a latitude of $b=55^\circ$. For the group at $\ell = 300^\circ$ and $\ell=270^\circ$, the theoretical values are lower than the observational value around $b = 70^\circ$. For the group at $\ell = 330^\circ$ and $\ell=240^\circ$, the theoretical values are lower than the observational values around $b = 75^\circ$ and $b = 55^\circ$, respectively.

In this paper, a power-law model is used to interpret the observations for the purpose of clarity. Models implemented with more complex physics, such as the Hernquist model (Newberg & Yanny 2005b), can fit the observations better. This could be one of the reasons that our model does not fit the observations perfectly. Modifications to this problem will be considered in a future study.

4.3 Fitting star counts in the $(g-r)$ colour

In the previous section, the projected surface number densities were fitted using a triaxial halo model. Star counts combined with colour information can, however, reveal more information about the stellar populations in the data and constrain the model better. Therefore, we performed model fits in the $(g-r)$ colour. The model described in Section 3 is now used to calculate star counts in the $(g-r)$ colour.

By using Eq. (1), the projected stellar number density in each absolute magnitude bin can be obtained. Monte Carlo simulations were carried out for absolute magnitude and distance, so that artificial stars could be generated for a given model, and hence theoretical apparent magnitudes could be generated. The $(g-r)$ colour as well as its statistical uncertainty at each point can then be obtained from the colour-magnitude relation.

Comparisons between the theoretical and observational star counts for all the fields were also done following Eq. (4). Subsequently, the $\chi^2_{(g-r)}$ values of all fields in the 12 groups were averaged to obtain the mean value $\overline{\chi^2_{(g-r)}}$. Intensive and elaborate computational tests were done for all possible cases. Each set of parameters represents a model which can be evaluated by its χ^2 and $\overline{\chi^2_{(g-r)}}$. It was found that χ^2 and $\overline{\chi^2_{(g-r)}}$ exhibit similar trends. However, when $\overline{\chi^2_{(g-r)}}$ reaches its minimum value, χ^2 may not be at its minimum. Therefore, we have to sacrifice minimizing the latter in order to keep $\overline{\chi^2_{(g-r)}}$ small. Table 5 lists the best-fit parameter combinations for power-law indices n from 2 to 2.6. Because of the six-dimensional parameter space, multiple solutions were derived. Fitting actual star counts in $(g-r)$ is much more difficult than fitting the projected surface number density. The minimum χ^2 value is about 1.735, but that of $\overline{\chi^2_{(g-r)}}$ is a few times higher. In our model, the power-law index n still leaves much room for fine-tuning, from 2.0 to 2.6 (beyond which χ^2 and $\overline{\chi^2_{(g-r)}}$ become too large). If constrained only by the projected number density (see Section 4.2), no firm constraint on the axial ratios (p, q) can be reached. When

supplemented with star counts in $(g-r)$, each n has only one best-fit (p, q) combination. For $n \leq 2.4$, (p, q) is (0.5, 0.5). This best-fit parameter set is different from that of the traditional axisymmetric model, even if $p = q$. In this model, the y axis is equal to the z axis, and therefore resembles the rotationally symmetric model, but with an inclination and tilt with respect to the Galactic plane. We would like to call all these $p = q$ cases also triaxial models. In such cases, good fits to the observational data can also be achieved. However, the ellipticity seems too oblate. When $n = 2.4$, (p, q) becomes (0.6, 0.5); when $n = 2.5$ or 2.6, (p, q) goes to (0.7, 0.6). The larger n becomes, the higher the axial ratio will need to be. Directly following from the power-law distribution, the number density decreases more rapidly for larger n when going away from the Galactic Centre. A higher axial ratio tends to enhance the number density in the directions of the axes. Hence, for larger n , a larger axial ratio is required to balance the effect of the larger n in order to fit the observational data. Such a correlation is the same as that for the direct surface number counts in Section 4.2.

Figs 6 and 7 show star counts in $(g-r)$ for the $b=60^\circ$ fields. The theoretical values were calculated with the same model as in Figs 4 and 5. Our purpose is to compare the mirror-symmetric pairs; four pairs of fields at approximately this latitude are considered. Because the sky field at $(30^\circ, 60^\circ)$ is not included in the survey, we chose the field at $(30^\circ, 65^\circ)$ to be paired with that at $(330^\circ, 65^\circ)$. The thin-line histogram represents the observational data, the solid black histogram describes the theoretical results. In Fig. 6, panel A shows the results for the sky field at $(0^\circ, 60^\circ)$, and panel B for $(180^\circ, 60^\circ)$. The panel pairs C-D, E-F, G-H and I-J are for four pairs of mirror-symmetric sky fields. Panel K in Fig. 7 is for the field at $(150^\circ, 60^\circ)$, a single field without a companion on the other side of the Galactic meridian plane. Comparing the observational data in the paired sky fields, the histograms for ℓ from 180° to 360° exhibit higher halo star peaks, and similar peaks for the thin disk with respect to those on the other side of the meridian. The theoretical model follows the same trend as the observations.

Apart from the problem of the structural parameters, the stars in the Galaxy are simplified as three populations (thin and thick disks, and halo), and it is further assumed that each population internally has the same age and metallicity. All of these assumptions will surely affect the distribution of the stars in the $(g-r)$ colour. A more precise g -band luminosity function and better partitioning of the populations are needed to interpret the continuously updating large-scale survey data.

5 DISCUSSION AND CONCLUSION

Star counts based on the observational data of the Milky Way analysed in the present paper show an asymmetry in the large-scale areas of the sky surrounding the northern Galactic pole, and therefore they reflect a certain non axisymmetric structure. These observations may be explained in one of two ways. The present smooth Galactic halo itself may have an asymmetric structure, which can be represented by a triaxial ellipsoid, possibly tracing the dark halo gravitational potential that might be triaxial (Jing & Suto 2002). The triaxiality proposed as such is not unique; it is

considered common for dark haloes in extragalactic systems. Mazzei & Curir (2001) analysed the effects of a triaxial dark halo on the bar-triggered star formation and feedback processes after the formation of the disk. They indicated that the dark halo has important effects on the evolution of baryonic matter. The star-formation rate is not only linked to the total mass of the dark halo, but also to the dynamical state of the dark halo. Is it then normal to form an asymmetric stellar halo in such an asymmetric gravitational field? In the history of formation and evolution of the Galaxy, the halo experienced accretion and merger processes. Wyse & Gilmore (2005) claim that merger events and accretion of satellite galaxies in the past history of the Galaxy do play some role in the evolution of the Milky Way. The outer halo, in particular, might be dominated by substructures that are likely the remnants of interactions. If the halo were very sparse originally and were gradually built up from accretion and merger events, it would be expected that there have been accretion events happening throughout the lifetime of the Milky Way. This would allow for any sizable features from early times to be smoothed out via dynamical evolution, leading to the formation of a smooth structure at the present time. Presumably, the star streams should have a random distribution due to the random infall angle and intensity, and therefore – on average – the overall features would have a smooth distribution after relaxation. Newberg and Yanny (2005b) selected F-type turn-off stellar data in eight SDSS stripes from the DR3 to map the distribution of stars in real space. They selected fields that most likely contain only halo stars. Sky areas near any previously identified overdensities caused by star streams were also avoided in their studies, but their results can be altered by the Virgo overdensity discovered later by Jurić et al. (2005). After they compared the observational data with the results of five triaxial models, they obtained the best-fit parameter set for an oblate ellipsoid with its major axis pointed at $50\text{--}70^\circ$ from the line of sight towards the Galactic Centre from the Sun, and with a $4\text{--}6^\circ$ inclination with respect to the Galactic plane. The minor axis, z , has a length equivalent to 65% of the major axis. The intermediate axis, y , is about 75% of the major axis (Newberg & Yanny 2005b).

An alternative cause of an asymmetric halo may be found in large-scale star streams that are embedded in the smooth background and that have not yet been melted into the halo completely. Also using DR4 data, Jurić et al. (2005) analysed the structure of the Galaxy using the photometric parallax method. They found that there are significant overdensities in the range ($5 < z/\text{kpc} < 15$), with the overdensity peaking in the direction of Virgo, and the entire overdensity region covers about one thousand square degrees on the sky. They selected both a sky field in the overdensity region and a control sky field mirror-symmetrically located on the other side of the meridian with respect to the target field, as shown in figure 24 of Jurić et al. (2005). By comparing stars with $0.2 < (g - r) < 0.8$ mag and $18 < r < 21.5$ mag in both fields, they estimated the surface brightness and luminosity of the overdensity in the target field as $\sum_r = 32.5$ mag arcsec $^{-2}$, and $L_r = 0.09 \times 10^6 L_\odot$. Based on this result, we can calculate the additional number of stars per square degree due to the overdensity. The magnitude range used by Jurić et al. (2005) spanned from $r = 18$ to 21.5 mag. Adopting the distance to the overdensity as 10 kpc, as also

assumed by Jurić et al. (2005), the lower and upper limit of the r -band absolute magnitude of their sample stars is therefore from 6.5 to 3 mag. From the transformation relation $r = V - 0.49(B - V) + 0.11$ (Chen et al. 2001), the limiting magnitudes in the V -band can be obtained (taking the $V - (B - V)$ relation for main-sequence stars from Cox 1999). The Mass – V magnitude relation from Reid (2002),

$$\log M = 0.477 - 0.135M_V + 1.228 \times 10^{-2} \times M_V^2 - 6.734 \times 10^{-4} M_V^3, \quad (5)$$

is used to calculate the mass of the most luminous ($1.45 M_\odot$) and the faintest stars ($0.81 M_\odot$) corresponding to the respective observed magnitude thresholds. Integrating the luminosity-mass ratio, weighed by $m \times \text{IMF}$ (Reid 2002), the additional stellar density number per square degree can be calculated,

$$N = L_{\text{tot}} / (c \int (L/m) m \phi(m) dm), \quad (6)$$

where c is the normalisation constant of the IMF. The derived number is 614 stars per square degree, which is indeed enough to match the number density excess with respect to a symmetric structure. However, this is still not enough to fully resolve the problem. By subtracting the CMD of a control field from that of the sky area characterised by the density excess, the flux of the Virgo star stream was derived. However, if a triaxiality does exist in the structure, there would be no proper criteria to distinguish the contribution due to the star stream from that of triaxiality.

As demonstrated in Fig. 4, there is a large region of stellar underdensity with respect to an axisymmetric model, which is centred at about $\ell = 150^\circ$ in the direction of Ursa Major (UMa) with an amplitude less than the Virgo overdensity. This was also shown in figure 3 of Newberg & Yanny (2005a), where they quote a minimum at $\ell = 155^\circ$ for F-type turn-off stars, very close to what we have found in this paper. The size of the UMa underdensity region is smaller than, but comparable to, that of the Virgo overdensity. The UMa underdensity is also clearly visible from figure 24 of Jurić et al. (2005; the blue colour-coded region near $\ell = 150^\circ$), and more prominently shown on the colour map in a recent news release on the SDSS web page. Such an underdensity region can also be found in the spatial distribution of M-giants from 2MASS observations (figure 27 of Jurić et al. 2005). The Virgo overdensity and the UMa underdensity regions are well aligned. If the overdensity is to be accounted for only by a star stream, what is then the cause for the observed underdensity aligned with it? This infers that there is some substructure within the halo that cannot be accounted for only by a star stream such as that of the Virgo overdensity. As shown in Fig. 4, the overdensity is observed in a very large region, from $\ell = 180^\circ$ to 360° , which is more than a quarter of sky at the latitude of $b = 60^\circ$. It cannot be fully understood by a stream covering only 1000 deg^2 . The triaxial halo model may provide a plausible explanation, because the distribution of the stellar surface number density at $b = 60^\circ$, including these over- and under-densities, can be fitted simultaneously by a triaxial halo model.

To disentangle the effects of a triaxial halo and the large-scale star stream, kinematic and chemical information is needed.

The substructures detected in the SDSS data are summarised in Table 2 of Newberg, Yanny & Rockosi (2002); two of their star streams pass through the sky fields selected in this study, namely S341+57–22.5 and S297+63–20.0. Since S341+57–22.5 is below the magnitude limits of the survey, it can hardly alter our results. S297+63–20.0 may have a minor influence on our results because of its limited size in the given direction. However, it will not change the general large-scale picture of the current work.

As the primary goal of the current work, a study of the large-scale structure of the Galactic halo using star counts is presented. The star streams can not easily be corrected for from the SDSS data. Therefore, we chose all-sky coverage to try to fit the average structure. We have shown that the stellar projected surface density of the halo stars at ℓ from 180° to 360° is significantly higher than that at ℓ from 0° to 180° at a latitude of 60° below the SDSS magnitude limit. The observed stellar projected surface density distributions in the sky fields selected for the current work can be well fitted by using a triaxial halo model. The parameter combinations of the best-fit triaxial models are, power-law index n from 2.0 to 2.6, θ from 55° to 65° , ϕ , ξ less than 5° , (p, q) either (0.5, 0.5), (0.6, 0.5), or (0.7, 0.6). These parameter sets agree with the one of Newberg & Yanny (2005b), except that their axial ratios are larger than ours. The results of the current work can still be affected by lumps in the star streams that have not yet been smoothly dispersed into the halo.

We are left with a number of questions, such as: what are the bulk of the stars in the star streams? What is the proportion of stars in the streams across the whole halo? Do star streams contribute significantly to the formation of a triaxial halo, or do they simply act as minor disturbances to the overall profile? How many of the star streams have already dispersed into the halo and become a smooth background, and how many of them can still be picked up from the smooth halo background? There is no way to have any clear answer for these questions from the present data. Work in this subject will leap forward with the coming on-line of future projects aimed at spectroscopic sky surveys such as SEGUE, LAMOST, SDSS II, GAIA, and further photometric surveys of the southern sky.

ACKNOWLEDGMENTS

We would like to thank B. Chen, Y. C. Liang, S. D. Mao, Z. G. Deng, X. Y. Xia, C. H. Du, Y. B. Yang, and Y. G. Wang for valuable suggestions and fruitful discussions. We are also very grateful for email communications with H. J. Newberg and A. Robin. We would like to thank our colleague, Dr. R. de Grijs, for proof reading the paper. This work is supported by the National Natural Science Foundation of China under grant No. 10333060, No. 10573022 and No. 10403006.

REFERENCES

- Bahcall, J. N., Soneira, R. M., 1980, *ApJS*, 44, 73
 Blitz, L., Spergel, D. N., 1991, *ApJ*, 370, 205
 Chen, B., Stoughton, C., Allyn Smith, J., et. al., 2001, *ApJ*, 553, 184
 Crawford, D. L., 1975, *AJ*, 80, 955
 Crawford, D. L., 1979, *AJ*, 84, 1858
 Deutschman, W. A., Davis, R. J., Schild, R. E., 1976, *ApJS*, 30, 97
 Drimmel, R., Cabrera-Lavers, A., López-Corredoira, M., 2003, *A&A*, 409, 205
 Fukugita, M., Ichikawa, T., Gunn, J. E., et. al., 1996, *AJ*, 111, 1748
 Gilmore, G., 1984, *MNRAS*, 207, 223
 Girardi, L., Grebel, E. K., Odenkirchen, M., et. al., 2004, *A&A*, 422, 205
 Gould, A., Bahcall, J. N., Flynn, C., 1996, *ApJ*, 465, 759
 Hartwick, F. D. A., 2000, *AJ*, 119, 2248
 Hayes, D. S., 1978, *proc. IAU Symp.*, 80, The HR diagram: The 100th anniversary of Henry Norris Russell, p. 65
 Houk, N., Cowley, A. P., 1975, *Michigan Catalogue of Two-Dimensional Spectral Types for the HD stars Vol. 1*, Univ Michigan, Ann Arbor
 Houk, N., Cowley, A. P., 1978, *Michigan Catalogue of Two-Dimensional Spectral Types for the HD stars Vol. 2*, Univ Michigan, Ann Arbor
 Houk, N., Cowley, A. P., 1982, *Michigan Catalogue of Two-Dimensional Spectral Types for the HD stars Vol. 3*, Univ Michigan, Ann Arbor
 Jing, Y. P., Suto, Y., 2002, *ApJ*, 574, 538
 Jurić, M., Ivezić, Ž., Brooks, A., et al., preprint (astro-ph/0510520)
 Kron, R. G., 1978, PhD thesis, University of California, Berkeley
 Larsen, J. A., Humphreys, R. M., 1996, *ApJ*, 468, 99
 Majewski, S. R., Siegel, M. H., Kunkel, W. E., et. al., 1999, *AJ*, 118, 1709
 Mazzei, P., Curir A., 2001, *A&A* 372, 803
 Newberg, H. J., Yanny, B., Rockosi, C., et. al., 2002, *ApJ*, 569, 245
 Newberg, H. J., Yanny, B., preprint (astro-ph/0502386)
 Newberg, H. J., Yanny, B., preprint (astro-ph/0507671)
 Parker, J. E., Humphreys, R. M., Larsen, J. A., 2003, *AJ*, 126, 1346
 Parker, J. E., Humphreys, R. M., Beers, T. C., 2004, *AJ*, 127, 1567
 Peterson, B. A., Ellis, R. S., Kibblewhite, E. J., et. al., 1979, *ApJ*, 233, L109
 Press, W. H., Teukolsky, S. A., Vetterling, W. T., et. al., 1992, *Numerical recipes in Fortran: the art of scientific computing*, Cambridge University Press, p. 616
 Reid, N., 1993, *ASPC*, 49, 37
 Reid, I. N., Yan, L., Majewski, S., et. al., 1996, *AJ*, 112, 1472
 Reid, I. N., 2002, *AJ*, 124, 2721
 Robin, A., Crézé, M., 1986, *A&A*, 157, 71
 Seares, F. H., 1925, *ApJ*, 61, 114
 Siegel, M. H., Majewski, S. R., Reid, I. N., et. al., 2002, *ApJ*, 578, 151
 Spergel, D. N., Blitz, L., 1988, *BAAS*, 20R1017S
 Stoughton, C., Lupton, R. H., Bernardi, M., et al., 2002, *AJ*, 123, 485
 Tyson, J. A., Jarvis, J. F., 1979, *ApJ*, 230, 153
 Wielen, R., 1974, *Highlights of Astronomy*, 3, p. 395, ed. G. Contopoulos
 Wielen, R., Jahreiss, H., kruger, R., 1983, in *Davis Phillip, A. G., Uppgren, A. R., eds, Proc. IAU Colloq. 76, Nearby*

Stars and the Stellar Luminosity Function, p. 163

Wyse, R. F. G., Gilmore, G., preprint (astro-ph/0510025)

Zheng, Z., Flynn, C., Gould, A., et al., 2001, ApJ, 555, 393

Zheng, Z., Flynn, C., Gould, A., et. al., 2004, ApJ, 601,
500

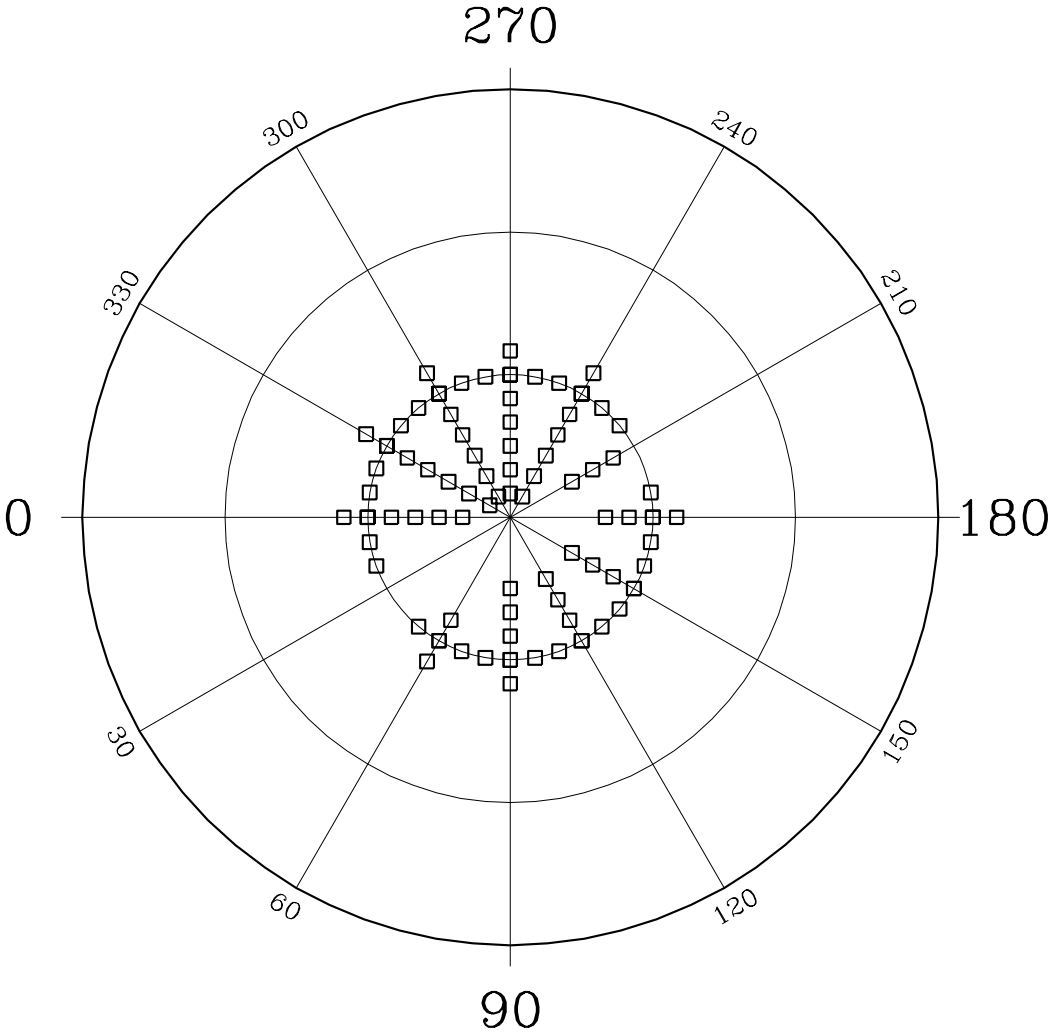


Figure 1. A sketch of the selected sky areas of the current study in Galactic coordinates.

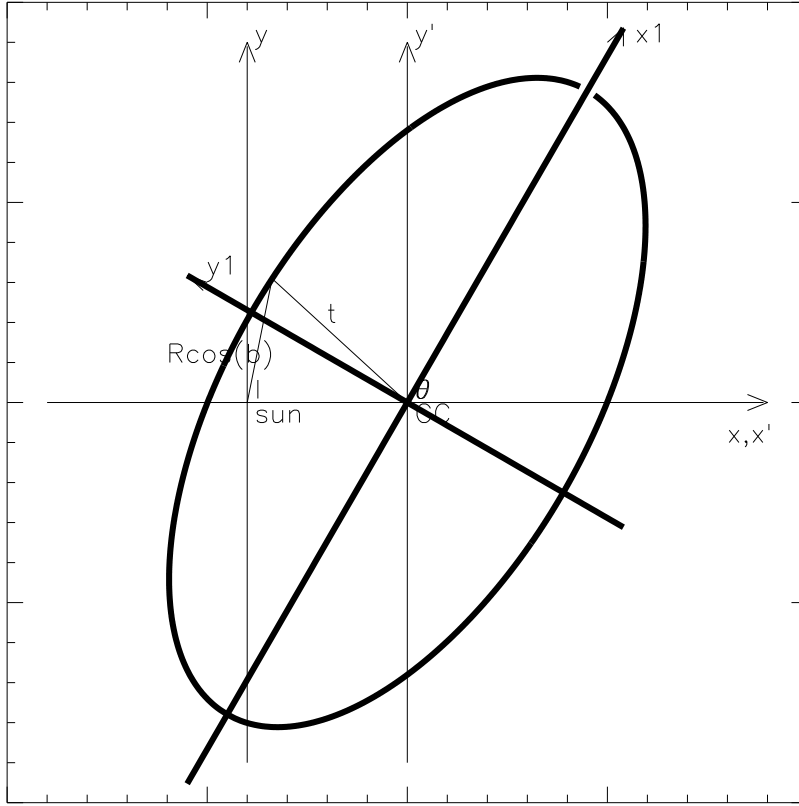


Figure 2. A sketch of the orientation of the coordinate frames.

Table 1. The Galactic coordinates of the selected sky fields in each group

group	(l,b)
1	(0°,60°),(10°,60°),(40°,60°),(50°,60°),(60°,60°),(70°,60°), (80°,60°),(90°,60°),(100°,60°),(110°,60°),(120°,60°),(130°,60°), (140°,60°),(150°,60°),(160°,60°),(170°,60°),(180°,60°),(190°,60°), (200°,60°),(230°,60°),(240°,60°),(250°,60°),(260°,60°),(270°,60°), (280°,60°),(290°,60°),(300°,60°),(310°,60°),(320°,60°),(330°,60°), (340°,60°),(350°,60°)
2	(0°,55°), (0°,60°), (0°,65°), (0°,70°)
3	(30°,65°), (30°,70°), (30°,75°)
4	(60°,55°), (60°,60°), (60°,65°), (60°,70°), (60°,75°), (60°,80°), (60°,85°)
5	(90°,55°), (90°,60°), (90°,65°), (90°,70°), (90°,75°),(90°,80°),(90°,85°)
6	(120°,55°), (120°,60°), (120°,65°), (120°,70°), (120°,75°),(120°,80°),(120°,85°)
7	(150°,55°), (150°,60°), (150°,65°), (150°,70°),(150°,75°), (150°,80°), (150°,85°)
8	(180°,55°), (180°,60°), (180°,65°), (180°,70°)
9	(240°,55°), (240°,60°), (240°,65°)
10	(270°,55°), (270°,60°), (270°,65°), (270°,70°), (270°,75°)
11	(300°,60°), (300°,65°), (300°,70°), (300°,75°)
12	(330°,60°), (330°,65°), (330°,70°), (330°,75°)

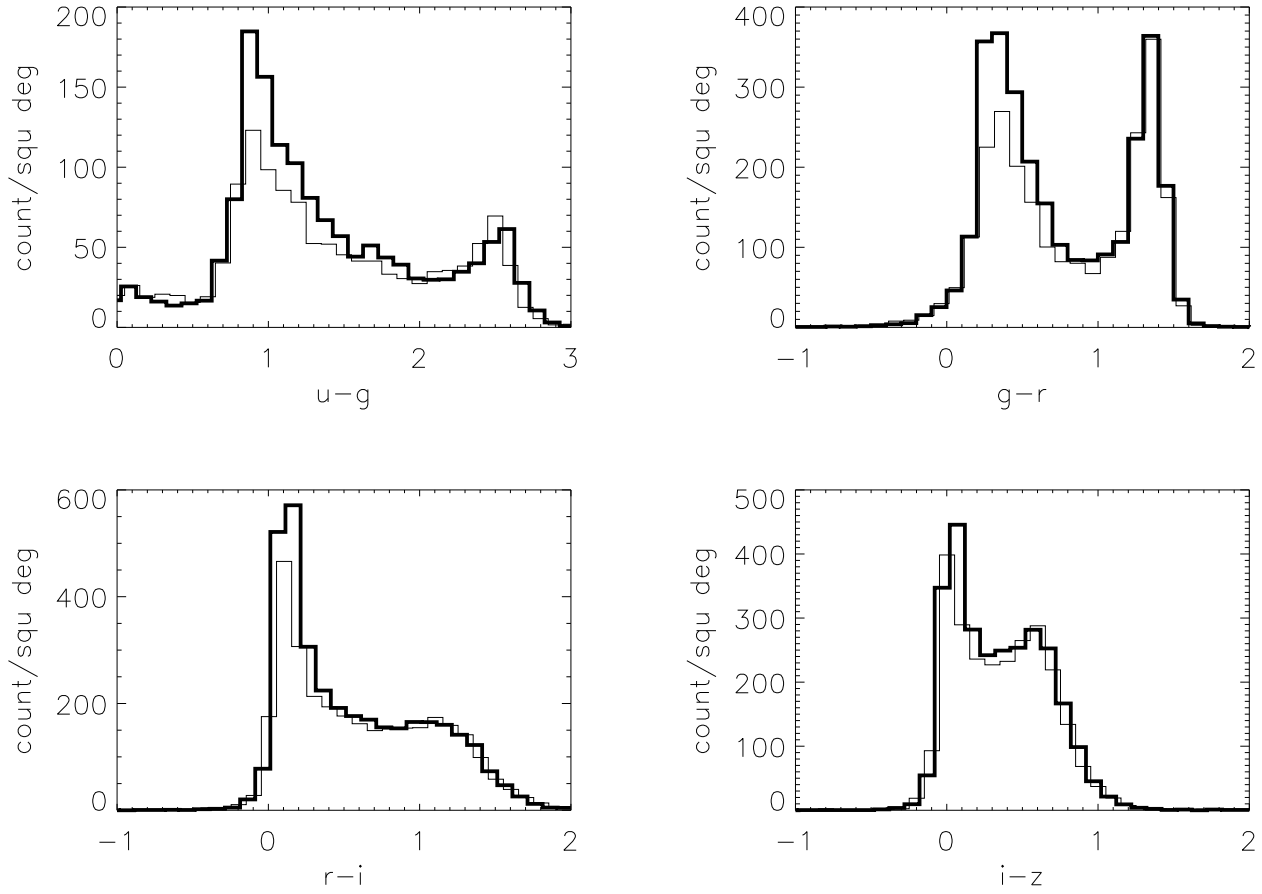


Figure 3. Star counts in four colors, namely $(u-g)$, $(g-r)$, $(r-i)$ and $(i-z)$. The thick solid histogram represents the star counts at $(270^\circ, 60^\circ)$, and the thin histogram describes star counts at $(90^\circ, 60^\circ)$; the two sky fields were chosen in mirror-symmetry with respect to the of $l=0^\circ$ Galactic meridian plane.

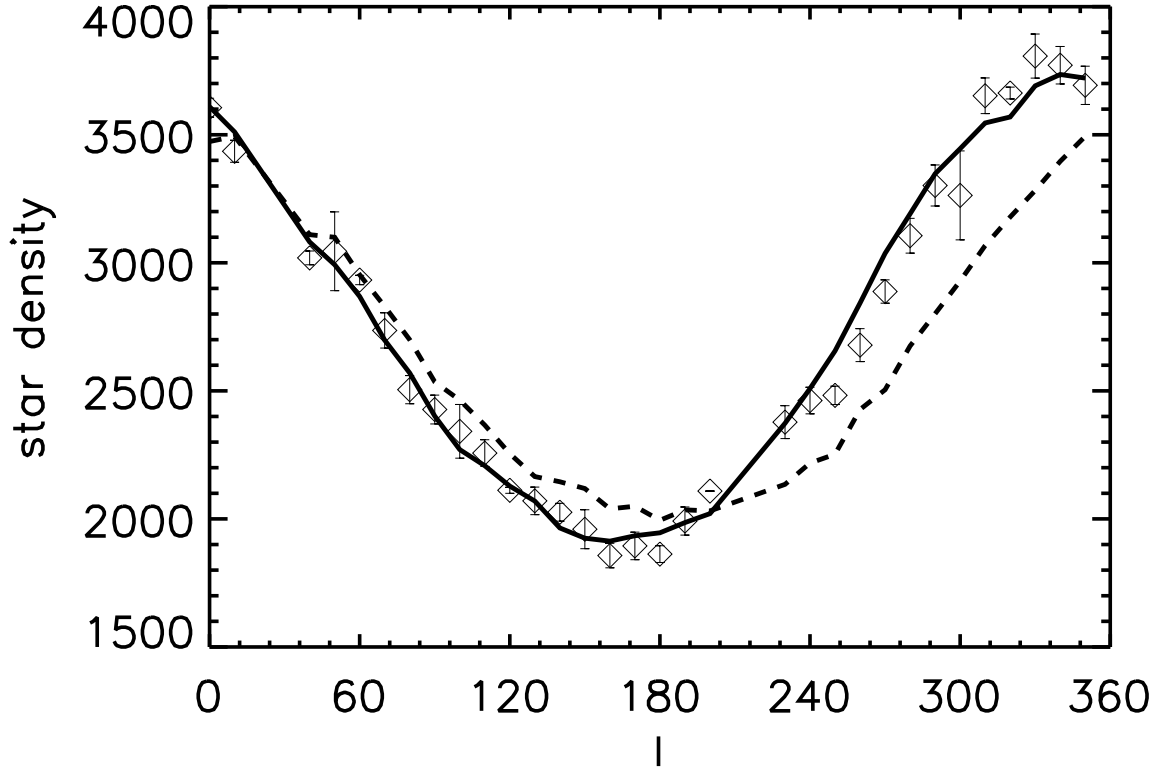


Figure 4. Stellar surface number density distribution at a latitude of 60° . The diamonds describe the surface number density of the observational data with g and r -band magnitudes from 15 to 22 mag; the error bars represent density fluctuations. The dashed line describes the theoretical result calculated based on an axisymmetric halo model, and the solid line describes the theoretical result for triaxial halo model.

Table 2. The relative deviations of the sky field pairs for $g, r \in [15, 22]$ mag. (see text for details).

ℓ_1 (degree)	ℓ_2 (degree)	asymmetry ratio(%)
10.000	350.000	7.49773
40.000	320.000	21.3195
50.000	310.000	19.9415
60.000	300.000	11.2650
70.000	290.000	20.6879
80.000	280.000	23.9994
90.000	270.000	18.9822
100.000	260.000	14.3713
110.000	250.000	9.98441
120.000	240.000	16.5926
130.000	230.000	14.8426
160.000	200.000	13.5624
170.000	190.000	5.12844

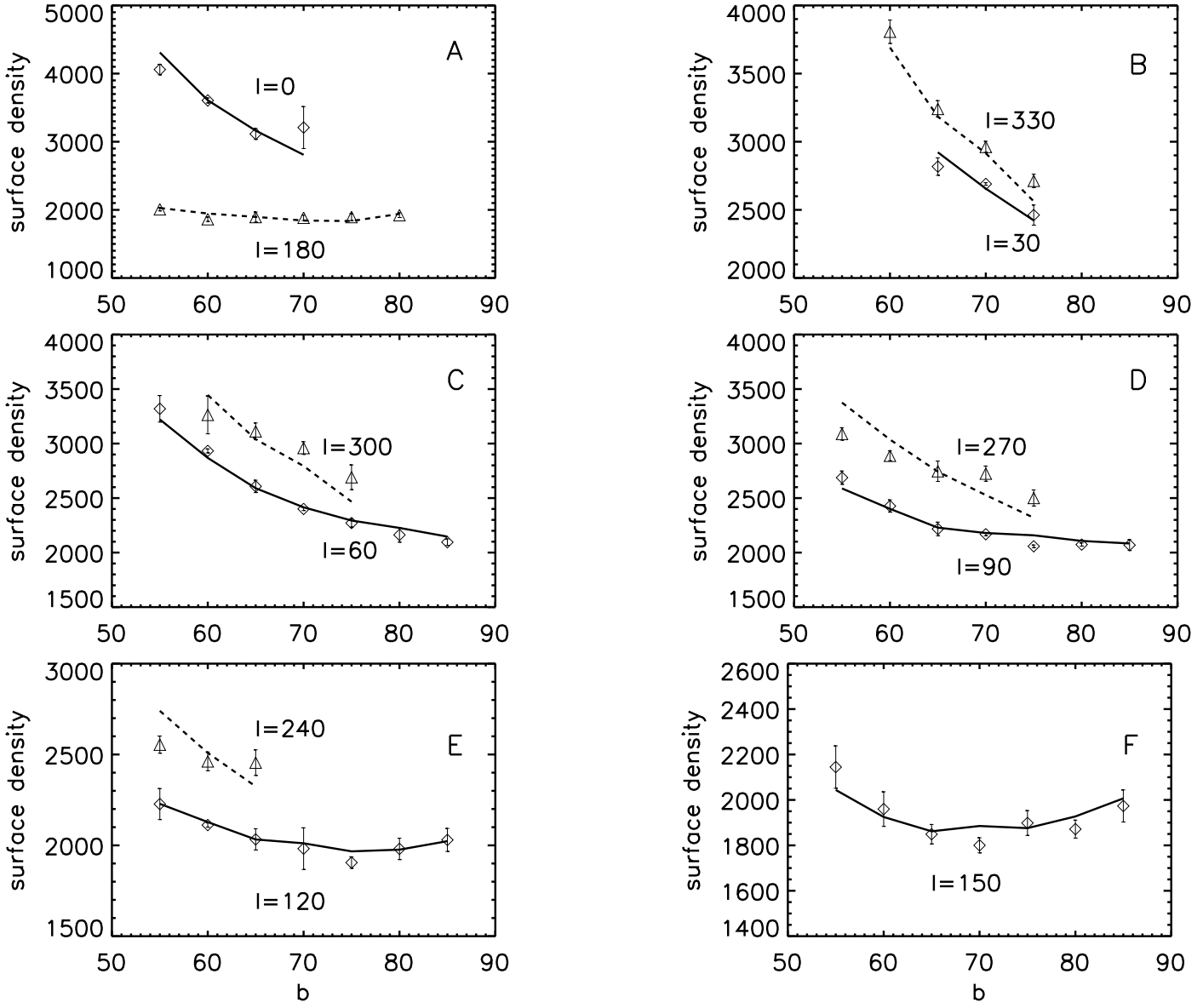


Figure 5. Fits of the surface number density using groups 2–12. The solid and dashed lines are the theoretical predictions, while the diamonds and triangles show the observational data. Panel A: solid line, diamond, $l=0^\circ$; dashed line, triangle, $l=180^\circ$. Panel B: solid line, diamond, $l=30^\circ$; dashed line, triangle, $l=330^\circ$. Panel C: solid line, diamond, $l=60^\circ$; dashed line, triangle, $l=300^\circ$. Panel D: solid line, diamond, $l=120^\circ$; dashed line, triangle, $l=240^\circ$. Panel E: solid line, diamond, $l=90^\circ$; dashed line, triangle, $l=270^\circ$. Panel F: solid line, diamond, $l=150^\circ$.

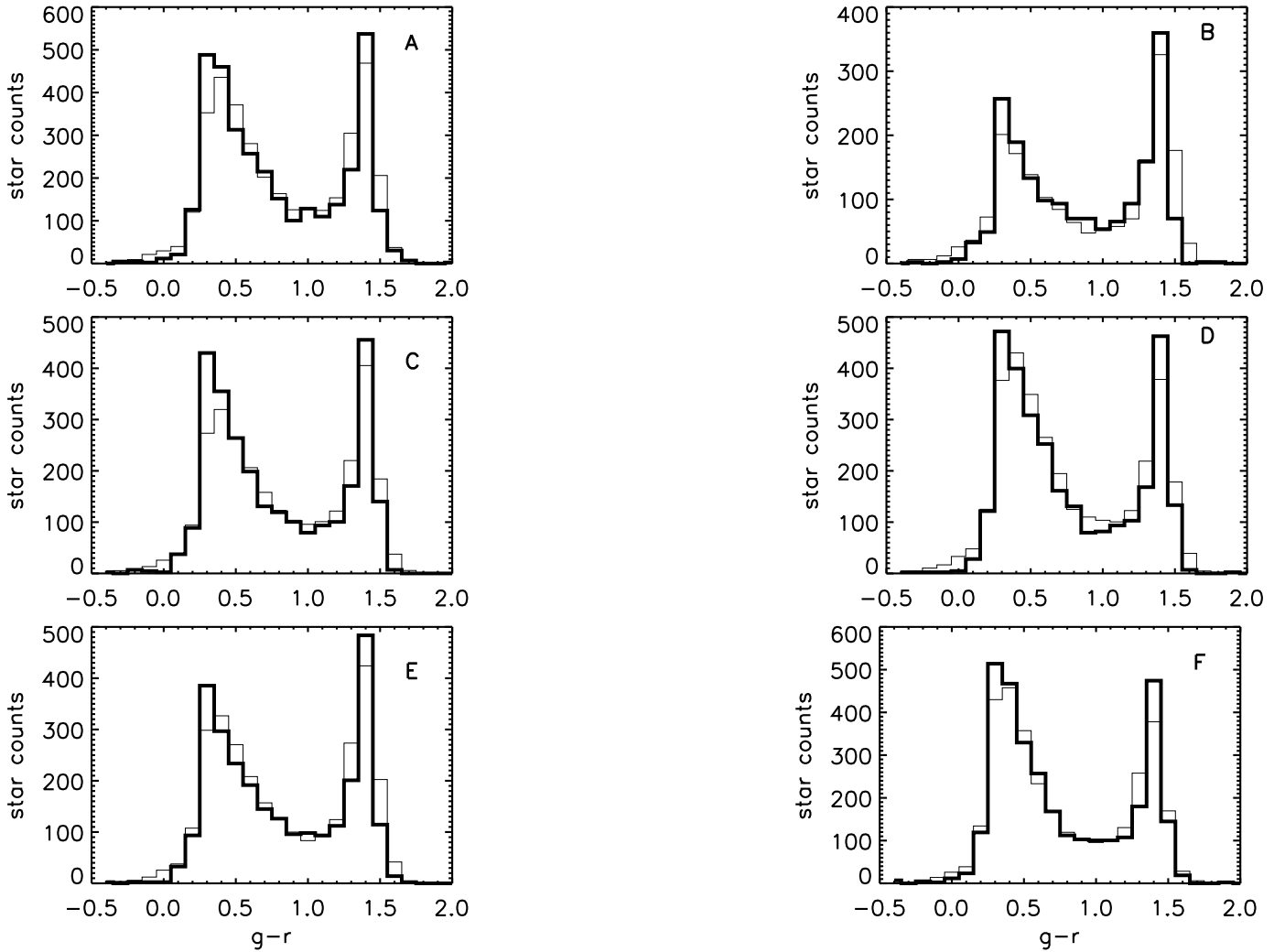


Figure 6. Fits of star count statistics in $(g - r)$ colour, where g and r are both within $[22, 15]$ mag. The thin lines describe the observational data, the solid black lines show the theoretical results. Panel A: the results for $(0^\circ, 60^\circ)$, Panel B: $(180^\circ, 60^\circ)$, Panel C: $(30^\circ, 65^\circ)$ Panel D: $(330^\circ, 65^\circ)$ Panel E: $(60^\circ, 60^\circ)$ Panel F: $(300^\circ, 60^\circ)$.

Table 3. The relative deviations of the sky field pairs, similar to Table 2 but for $g, r \in [19, 21]$ mag.

ℓ_1 (degree)	ℓ_2 (degree)	asymmetry ratio(%)
10.000	350.000	10.2431
40.000	320.000	32.7824
50.000	310.000	26.8430
60.000	300.000	24.9343
70.000	290.000	35.5734
80.000	280.000	33.3278
90.000	270.000	29.9915
100.000	260.000	26.4650
110.000	250.000	15.3487
120.000	240.000	16.3516
130.000	230.000	12.8257
160.000	200.000	19.2948
170.000	190.000	5.18586

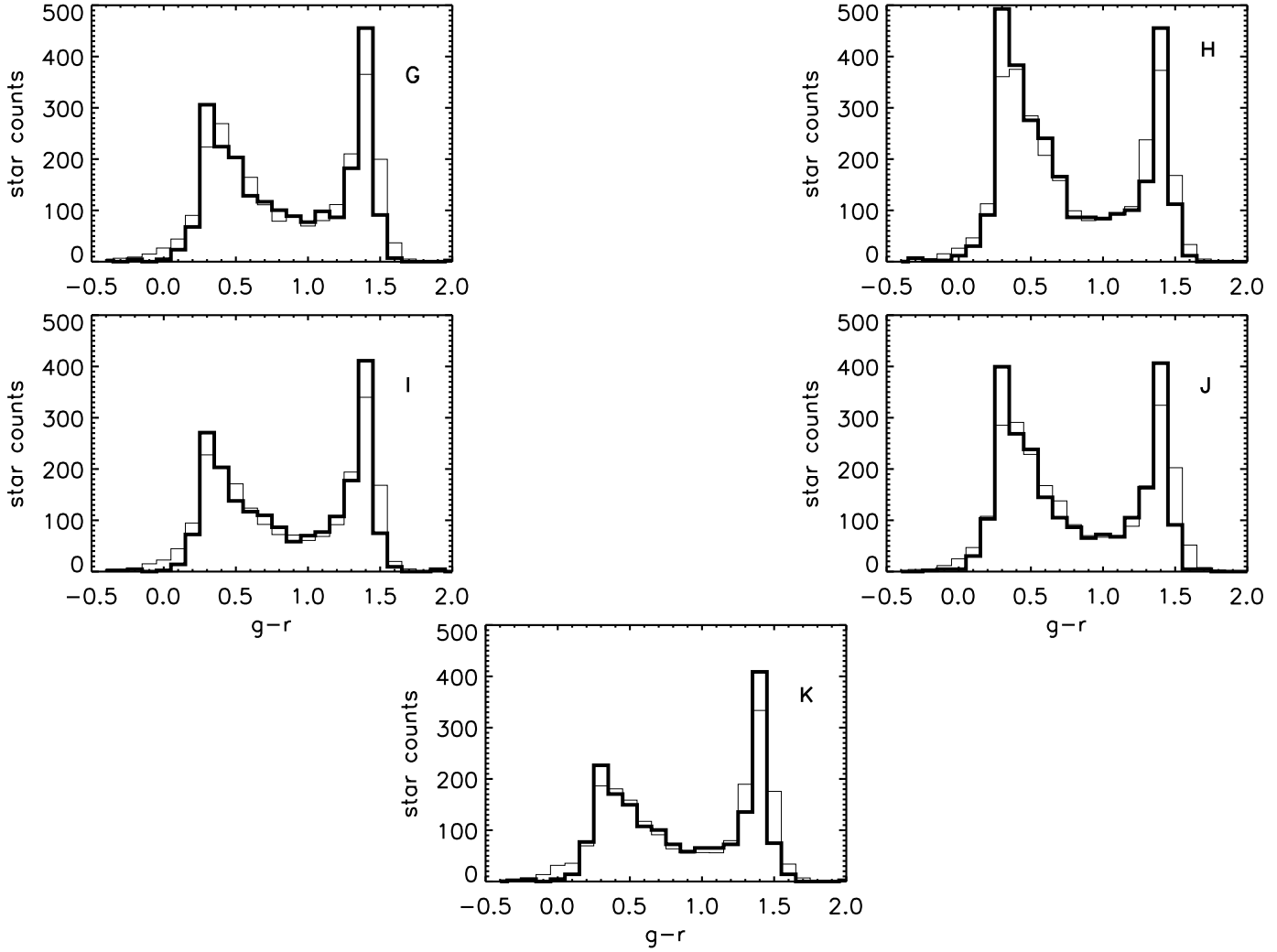


Figure 7. -continued. Panel G: ($90^\circ, 60^\circ$), Panel H: ($270^\circ, 60^\circ$), Panel I: ($120^\circ, 60^\circ$) Panel J: ($240^\circ, 60^\circ$), Panel K: ($150^\circ, 60^\circ$)

Table 4. Input ranges of the parameters.

parameter	lower limit	upper limit	step
n	2	3	0.1
p	0.5	0.9	0.1
q	0.5	0.9	0.1
θ	55°	65°	5°
ξ	-20°	5°	5°
ϕ	-20°	5°	5°

Table 5. The best-fit parameters for fixed power-law index n at [2,2.6]

power-law index	θ (degree)	p	q	ξ (degree)	ϕ (degree)	χ^2	$\overline{\chi^2}_{(g-r)}$
2.	65.	0.5	0.5	-15.	-5.	2.302	7.092
2.1	65.	0.5	0.5	-20.	-10.	1.735	6.842
2.2	60.	0.5	0.5	-10.	-10.	2.02	6.632
2.3	55.	0.5	0.5	5.	-15.	2.869	6.909
2.4	65.	0.6	0.5	5.	-20.	2.965	7.073
2.5	65.	0.7	0.6	-15.	-10.	3.055	7.204
2.6	65.	0.7	0.6	-15.	-10.	3.539	7.257